Article

Enhancement of Mechanical Behaviors and Microstructure Evolution of Nano-Nb$_2$O$_5$/AZ31 Composite Processed via Equal-Channel Angular Pressing (ECAP)

Song-Jeng Huang [1],*, Sathiyalingam Kannaiyan [2],*, Manas Sarkar [1] and Matoke Peter Mose [1]

1   Department of Mechanical Engineering, National Taiwan University of Science and Technology,
     No. 43, Section 4, Keelung Rd, Da'an District, Taipei 10607, Taiwan; sarkarmanas72@gmail.com (M.S.);
     peter.mose022@gmail.com (M.P.M.)
2   Department of Aeronautical Engineering, Dhanalakshmi Srinivasan Engineering College, Thuraiyur Road,
     Perambalur 621212, India
*   Correspondence: sgjghuang@mail.ntust.edu.tw (S.-J.H.); sathiaerospace@gmail.com (S.K.)

Abstract: The automobile industry uses magnesium for load-bearing components due to its low density, durability, and ductility. This study investigated a nanocomposite containing Nb$_2$O$_5$ (3 and 6 wt%) nanoparticles as reinforcement with AZ31 magnesium alloy made by stir casting. A severe plastic deformation was conducted on the cast samples via equal-channel angular pressing (ECAP) after homogenization at 410 °C for 24 h and aging at 200 °C for 10 h. The microstructural distributions and mechanical properties of the magnesium metal matrix composites (MMCs) reinforced with Nb$_2$O$_5$ nanoparticles were investigated via ECAP. With the increase in the number of ECAP passes, the grain sizes became uniform, and the size of secondary phases reduced in the pure Nb$_2$O$_5$/AZ31 MMC. The grain size decreased remarkably after the ECAP process from 31.95 μm to 18.41 μm due to the dynamic recrystallization during plastic deformation. The mechanical properties of hardness, ultimate tensile strength, and elongation effectively improved after each ECAP pass. The maximum values achieved for the Nb$_2$O$_5$/AZ31 composite subjected to ECAP were 64.12 ± 12 HV, 151.2 MPa, and 52.71%.

Keywords: nanocomposites; microstructures; ductility; dislocations; fractography

1. Introduction

Many countries have started to focus on carbon neutrality and emission peak strategies since 2020. Nowadays, the carbon neutrality and emission peak strategies of many countries include the transition from ICEs to electric vehicles. Weight reduction helps reduce fuel/electricity consumption and also increase the travel range, which is key for electric vehicles (e.g., see article 'Cost, range anxiety and future electricity supply: A review of how today's technology trends may influence the future uptake of BEVs') [1]. The extensive use of magnesium can be one of the best solutions to reduce these problems [1–3]. Weight reduction can lead to many advantages, such as reduction in carbon dioxide emission due to less fuel consumption in the automotive industry [4,5]. In the automotive industry, magnesium alloys (Mg-Al-Zn) are widely used because they have good corrosion resistance and excellent die-casting abilities and can be used at room temperature. As a result, this alloy can be found in crankcases, steering boxes, steering columns, brake pedals, transmission cases, engine cradles, steering wheel cores, oil pump housings, and other components [6]. The most important factor that makes magnesium alloys suitable for use is their density. They are two-thirds less dense than aluminum, but their strength, creep, and corrosion resistance are comparatively lower than aluminum alloys, which must be improved. This mechanical property improvement requires several techniques, such as heat treatment, cold work, and thermomechanical forming. The features of magnesium alloy that can

be manipulated and improved are the grain size, coefficient of thermal expansion, and precipitation processes [7]. Grain refinement can be a solution to improve the mechanical properties. It improves the mechanical properties, and the paradox of strength and ductility is eliminated by achieving ultrafine grain [8,9].

Various fabrication methods, such as squeeze casting, powder metallurgy, spray deposition, stir casting, and physical vapor deposition, have been introduced and are used in industries at present [10–14]. Among the casting techniques, stir casting has some advantages, such as economic feasibility, large-scale casting capacity, and considerable flexibility [11,15]. In this study, stir casting was used to cast AZ31 with nano-Nb_2O_5 as reinforcement. As reinforcements approach the nano scale, their properties change. Since nanoparticles are so small, they have a very high surface area-to-volume ratio in comparison to bulk materials. When the reinforcement phase is reduced to a nano-scale, particle interaction with dislocations becomes increasingly significant, which results in a remarkable increase in mechanical properties when combined with other strengthening effects typically seen in conventional metal matrix composites. The properties of Nb_2O_5 include excellent thermal, chemical, and thermodynamic stability, high reflective indices, excellent mechanical properties, and excellent fracture toughness. The superior catalytic property of Nb_2O_5 enables hydrogen absorption and desorption, along with biomedical and sensor applications [16]. Heat treatment, forging, and rolling are some of the secondary processing methods employed to improve strength and ductility. The combination of aging and severe plastic deformation (SPD) with equal-channel angular pressing (ECAP) effects has been proposed to improve the mechanical behavior [17]. Finer grain sizes can be achieved through SPD [18]. ECAP is a more concentrated SPD method for refining grain size in bulk materials [19–21]. In a study by Feng et al. [22], discontinuous precipitates were observed at the grain boundaries of Mg–Zn–Al alloys during aging. ECAP can improve and modify the mechanical properties of engineering alloys, depending on the channel geometry and the number of passes. Researchers investigated the ECAP effects of AZ91 reinforced with SiCp and found that the grain size reduces after four passes [23]. The microstructural and mechanical properties of AZ31 and ZK60 were investigated by focusing on various parameters, such as initial condition, material type, die angle, and number of ECAP passes. They concluded that ultrafine grain can be obtained in one ECAP pass if the initial grain size of the inserted material is fine [24]. In order to achieve a significant impact on the microstructure and mechanical properties of high-performance materials, the processing routes may vary depending on how the billet is rotated [25]. ECAP has several routes, such as A, B_c, and C. The rotational approaches are as follows: route A: no rotation of the billet; route B_C: rotation of the billet 90° clockwise; route B_A: rotation of the billet 90° clockwise and counterclockwise consecutively; and route C: rotation of the billet 180°. However, the texture has a remarkable difference depending on the various routes, and the intensity of the textural component is different for different ECAP routes. The selection of a suitable route path is extremely important and is based on the material [26]. The suitable ECAP path for AZ31 magnesium alloy to achieve a better-than-expected result is route B_c. According to Muralidhar Avvari et al. [27], the B_c route provides the maximum deformation for AZ31 compared with routes A and C due to the strain path variation that influences the grain size refinement in the material. As a result of SPD processing, magnesium alloy grains are smaller than those in conventionally processed alloys, resulting in enhanced superplasticity in Mg alloys [28]. An investigation on AZ61 magnesium alloy found that the increase in the number of passes enhanced the uniform microstructural distribution that increases ductility. However, the properties, such as strength, ductility, and strain hardness, of 2 wt% SiCp/AZ61 Mg MMCs increased, whereas the opposite result was observed in the case of 5 wt% SiCp/AZ61 due to the clustering of SiC and Mg_2Si secondary phase [29,30].

The novelty in the current research is Nb_2O_5 as a new reinforcement considered for the fabrication of magnesium metal matrix composites. It should be noted that none of the studies examined the fracture properties and microstructure of magnesium alloy composites reinforced with Nb_2O_5 and more specifically with the ECAP process. The objective of this

research is to study the ECAP effects on the mechanical characteristics of AZ31 composites with varying Nb_2O_5 weight fractions. All characterization investigations were performed to reveal the successful incorporation of $AZ31/Nb_2O_5$ composite and its properties.

2. Experimental Procedures

Composite Preparation

The AZ31 magnesium alloy was bought from Kuangyue Co., Ltd.,Taiwan and Ally-chem Company Ltd. China supplied the 99.90 percent pure Nb_2O_5 that was used as a reinforcement in the composite material. The size of the Nb_2O_5 particles that were selected was 100 nm. The composition of AZ31 alloy shown in Table 1.

Table 1. Magnesium AZ31 alloy composition (wt%).

Mg	Al	Zn	Mn	Si	Cu	Ca	Fe
95.42	3.2	0.9	0.3	0.1	0.04	0.03	0.005

The composite ingots were made through a process known as gravitational mechanical stir casting, and they were made with three distinct types of composition. The three types of composition are as follows: AZ31-0 wt % Nb_2O_5 (AZ31), AZ31-3 wt % Nb_2O_5 (3 wt% $Nb_2O_5/AZ31$), and AZ31-6 wt% Nb_2O_5 (6 wt% $Nb_2O_5/AZ31$). A gravimetric resistance furnace with protective agents ($SF6 + CO_2$) was used for the casting of the ingots. The molten mixture was stirred for 15 min at 760 °C to produce a composite material and obtain the maximum possible homogeneous dispersion of nano Nb_2O_5 in the AZ31 matrix. An argon gas working atmosphere was utilized to prevent the occurrence of oxidation and burning. The crucible had a mold placed underneath it so that the liquid mixture could cool and solidify into ingots when it was brought to room temperature [31].

The ingots served as the starting material for the production of the billets, which had dimensions of $11.5 \times 11.5 \times 75$ mm (Figure 1a). The billets were quenched in water after homogenization for 24 h at 400 °C. The samples underwent aging for 10 h at a temperature of 200 °C, and the temperature of the furnace was lowered until the room temperature was reached. The samples were then allowed to cool down gradually. During the ECAP process, the billet was allowed to remain inside the die for a period of 40 min at a constant temperature of 350 °C to produce uniform heat dispersion. The billets were deformed by using a plunger at a speed of 15 mm/min and an internal angle of 120°. For all the samples used for microstructural and mechanical characterization, as shown in Figure 1b, the samples were ground by using silicon carbide paper of varying grit sizes. The grain boundaries in the specimens were brought to light by polishing them with fine polishing paper and alumina solution. The polished samples were etched with 100 mL of ethanol, 10 mL of DI water, 5 mL of acetic acid, and 6 g of picric acid solution for 40 s before performing microstructure analysis. A scanning electron microscope (SEM) with energy dispersive spectroscopy (model number JSM-6390LV) was utilized to investigate the fracture and microstructure characteristics. A Bruker D2 phase X-ray diffractometer operating at 35 kV and 40 mA with Cu-K radiation was utilized to explore the phase composition of the composites. D (nm) is the crystallite size, calculated through the Scherer equation: $D = k\lambda/\beta cos\theta$, where 2θ is peak position and β is its corresponding FWHM. These two parameters are calculated directly through Origin software from XRD data. δ (nm^{-1}) is the dislocation density. $\delta = 1/D2$ is the equation for the calculation of its value. Tensile samples in the shape of a dog bone were made in compliance with the ASTM-E8-69 requirements (Figure 1a), and a universal testing machine was used to evaluate the mechanical behavior of the composites (MTS-100KN) operated at a 0.5 mm/min deformation rate at room temperature. Three tensile samples were considered for each set of experiments. The microhardness was measured at 300 gmf with a 10 s dwell time by using a Vickers hardness tester (Akashi MVK-H1).
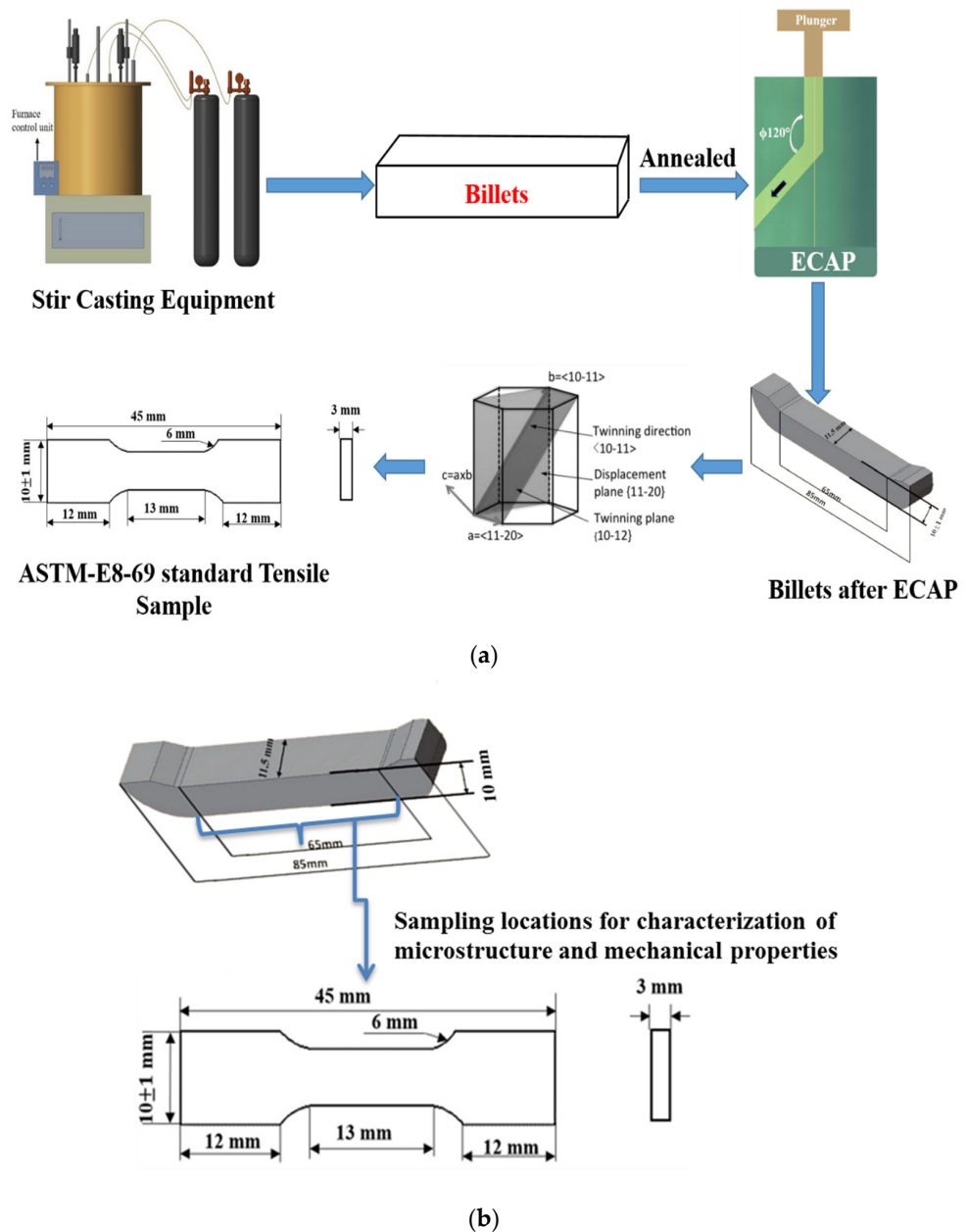
Figure 1. (**a**) Schematic diagram of the experimental setup. (**b**) Sampling locations for characterization of microstructure and mechanical properties.

3. Results

3.1. Microstructure Characteristics

The SEM images (Figure 2) show that the grain sizes and microstructure distributions of the Nb_2O_5/AZ31 composites are more uniform after being subjected to the ECAP plastic deformation processes. A reduction in $Al_{12}Mg_{17}$ secondary phase sizes was observed in the AZ31 magnesium alloy because more ECAP passes were made. The quantitative value of the $Al_{12}Mg_{17}$ secondary phase changed with the increase in ECAP passes, as determined by analyzing the X-ray diffraction (XRD) quantitative phase data for the composite results of one and two passes. The values for the first and second passes were 0.9% and 0.7%, respectively. Secondary phases, such as $Al_{12}Mg_{17}$, have an effect on the strength of magnesium alloys and have a detrimental effect on their ductility. As shown in Figure 3A–C, an elemental analysis was performed by using EDS on the composite that was aged and ECAPed composite. The findings of this study indicated that the Nb_2O_5

particles were evenly distributed in grain boundaries, indicating the presence of the major element magnesium. The minor alloying elements of aluminum and zinc were distributed throughout the grain evenly.
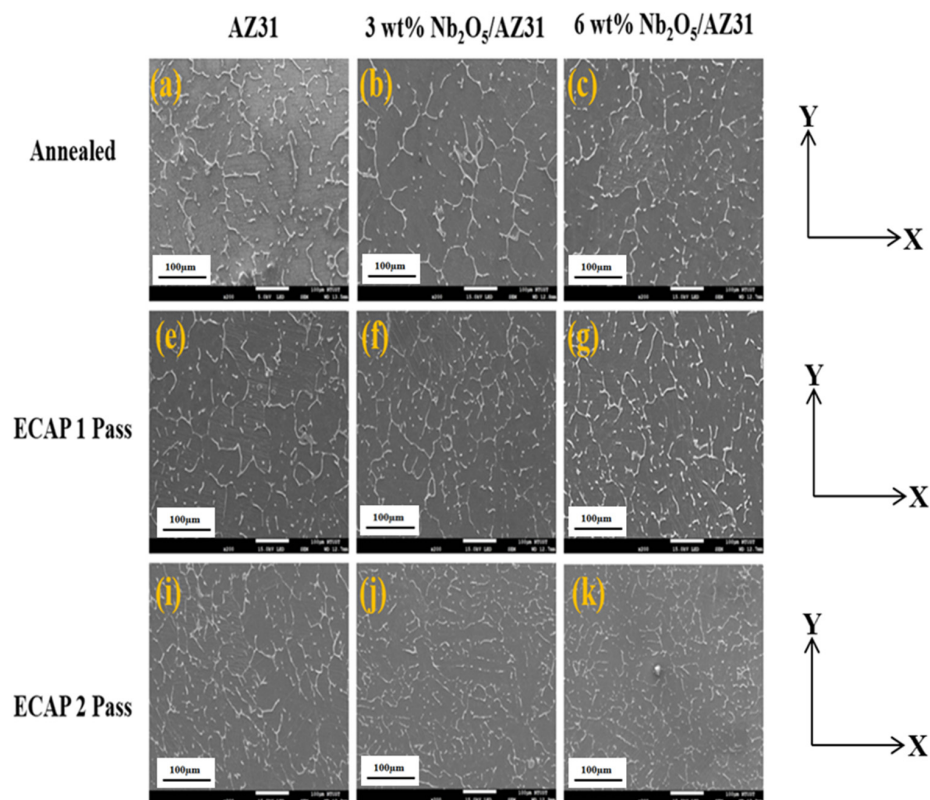

Figure 2. SEM analysis images of annealed (**a**–**c**), ECAP 1-pass (**e**–**g**), and ECAP 2-pass (**i**–**k**) composite.
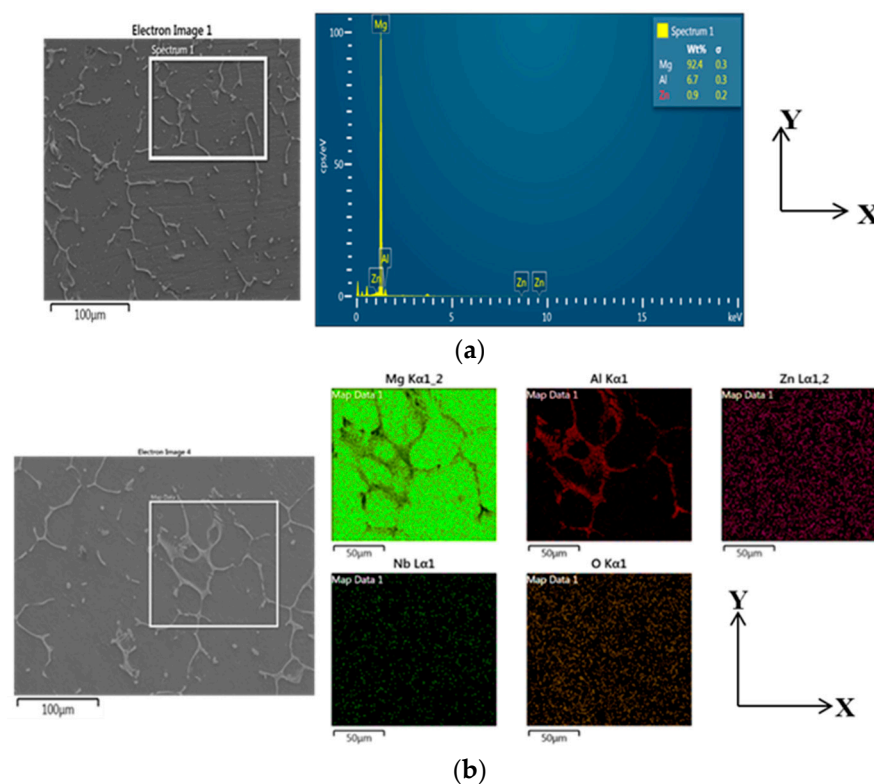

Figure 3. *Cont.*

(**c**)

(**A**)

(**B**)
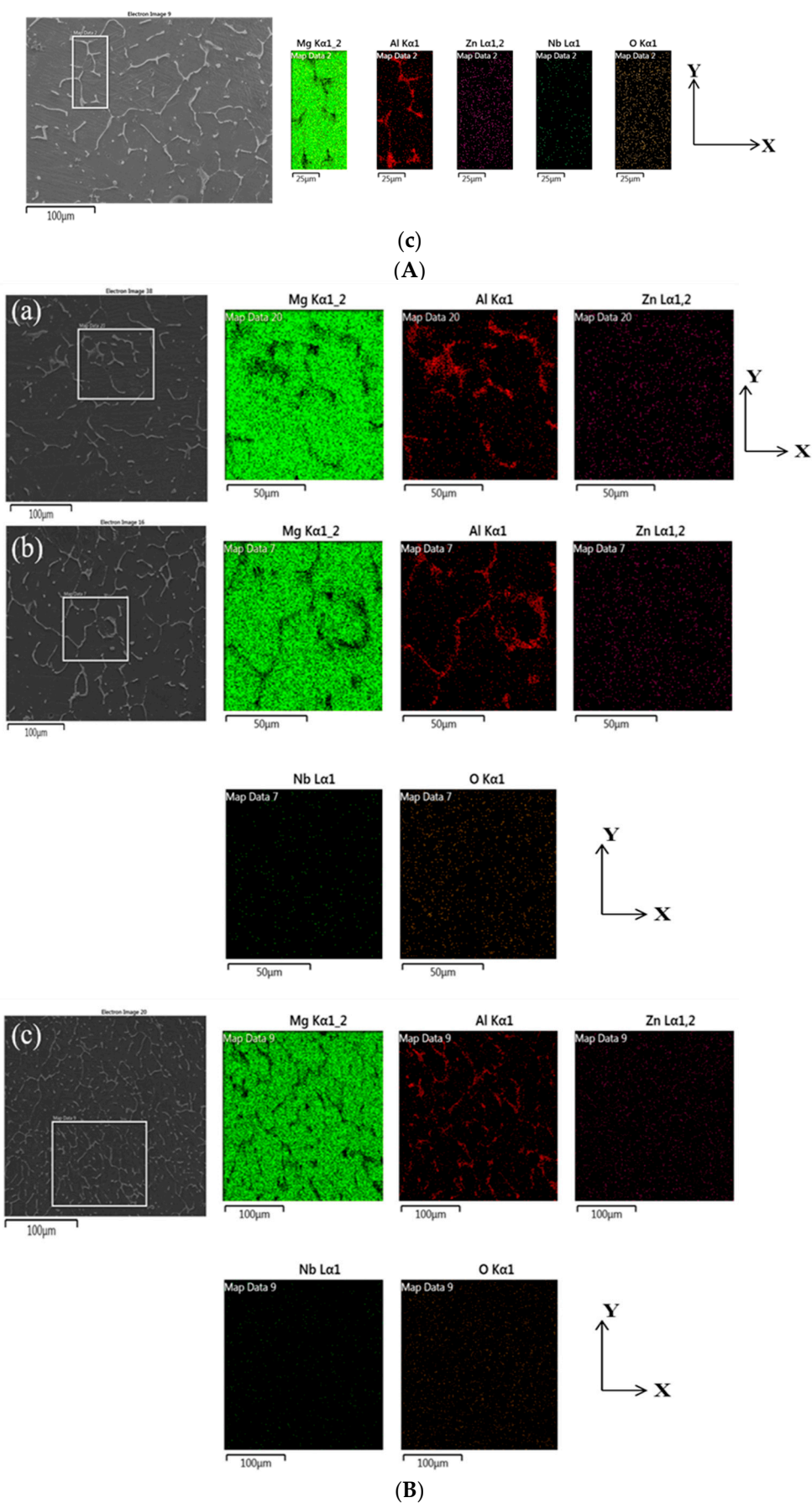
Figure 3. *Cont.*
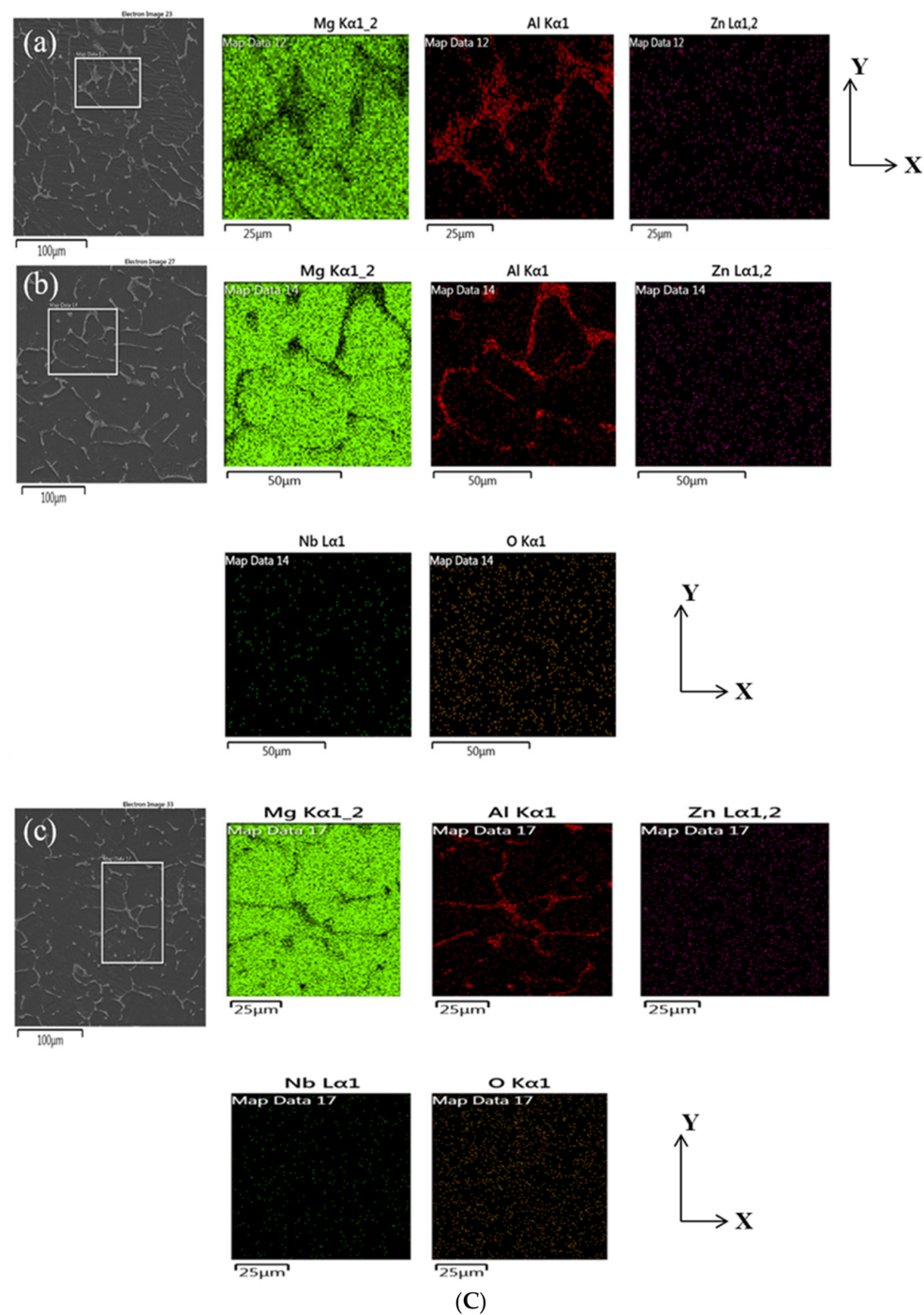
Figure 3. (**A**). EDS mapping images of annealed samples: (**a**) AZ31, (**b**) 3 wt% Nb_2O_5/AZ31, (**c**) 6 wt% Nb_2O_5/AZ31. (**B**). EDS mapping images of ECAP 1-pass samples: (**a**) AZ31, (**b**) 3 wt% Nb_2O_5/AZ31, (**c**) 6 wt% Nb_2O_5/AZ31. (**C**). EDS mapping images of ECAP 2-pass samples: (**a**) AZ31, (**b**) 3 wt% Nb_2O_5/AZ31, (**c**) 6 wt% Nb_2O_5/AZ31.

3.2. XRD Analysis

XRD plots are shown in the figure for aged and ECAPed composites. From the graph, it is apparent that there is a presence of the Mg matrix, indicated by the occurrence of major peaks around 32, 34, and 37 degrees (PDF 65-4596) and scattered minor peaks. Additionally, peaks at $32.4°$ (PDF 38-1459) and $36°$ (PDF 73-1148) were identified as evidence of $Mg_{17}Al_{12}$ and $Mg_4Nb_2O_9$, respectively. With the exception of minor peaks, the plots were similar to those of the base AZ31 alloy. It was also noted that $Al_5Mg_{11}Zn_4$ and Al_3Mg_2 phases exhib-

ited diffraction peaks at 36.8° (PDF 50-1502) and 37.5° (PDF 29-0048), respectively. Phase quantification of annealed and ECAPed $Nb_2O_5/AZ31$ composites are shown in Table 2.

Table 2. Phase quantification of annealed and ECAPed $Nb_2O_5/AZ31$ composites.

Major Phases	AZ31	3 wt% Nb_2O_5/AZ31	6 wt% Nb_2O_5/AZ31
Annealed			
$Mg_{0.97}Zn_{0.03}$	24.9	19.4	19.6
$Al_{12}Mg_{17}$	0.9	0.6	0.6
Al_3Mg_2	6.1	4.6	4.5
$Al_5Mg_{11}Zn_4$	68.1	52.4	52
$Mg_4Nb_2O_9$	-	23	23.3
ECAP-1 Pass			
$Mg_{0.97}Zn_{0.03}$	25.4	19.3	19.4
$Al_{12}Mg_{17}$	0.7	0.6	0.6
Al_3Mg_2	6	4.7	4.8
$Al_5Mg_{11}Zn_4$	67.9	52.4	52.6
$Mg_4Nb_2O_9$	-	23	22.6
ECAP-2 Passes			
$Mg_{0.97}Zn_{0.03}$	25.7	19.1	19.1
$Al_{12}Mg_{17}$	0.7	0.7	0.6
Al_3Mg_2	6	4.9	4.9
$Al_5Mg_{11}Zn_4$	67.6	53	51.3
$Mg_4Nb_2O_9$	-	22.3	24.1

3.3. Microhardness

The microhardness values of $Nb_2O_5/AZ31$ MMCs processed using ECAP are shown in Table 3. Compared with aged composite, ECAPed $Nb_2O_5/AZ31$ composites exhibited an improvement in microhardness. The hardness of the reinforced composite increased marginally as the volume fraction of the reinforcement particles increased. The microhardness value of 3 wt% $Nb_2O_5/AZ31$ increased by 4.7% and 5.8% for one and two passes compared with the annealed composite. Similarly, the microhardness value of 6 wt% $Nb_2O_5/AZ31$ increased by 5% and 4% for and 1 and 2 passes compared with the aged composite.

Table 3. Mechanical properties of annealed and ECAPed $Nb_2O_5/AZ31$ composites.

Composition	Crystallite Size (µm)	Degree of Crystallinity (%)	Microhardness (Hv)	Ultimate Tensile Strength (MPa)	Young's Modulus (MPa)	Elongation %
Annealed						
AZ31	31.95	62.08	59.24 ± 7.12	131.7 ± 2.12	5528.6	15.01 ± 5.60
3 wt% Nb_2O_5/AZ31	34.38	70.60	62.68 ± 6.60	142.9 ± 3.60	5784.1	20.47 ± 4.34
6 wt% Nb_2O_5/AZ31	37.15	72.92	60.88 ± 7.10	136.8 ± 2.05	5715.5	17.09 ± 2.48
ECAP 1 Pass						
AZ31	29.29	59.77	58.83 ± 5.17	135.8 ± 4.60	5415.0	33.69 ± 4.81
3 wt% Nb_2O_5/AZ31	26.034	64.978	63.21 ± 6.71	149.6 ± 4.25	6385.8	52.71 ± 3.35
6 wt% Nb_2O_5/AZ31	27.12	68.360	61.83 ± 4.19	143.7 ± 3.70	5971.4	45.59 ± 4.10
ECAP 2 Passes						
AZ31	18.41	63.325	63.01 ± 5.69	138.5 ± 4.33	4626.84	15.05 ± 3.05
3 wt% Nb_2O_5/AZ31	19.38	80.47	64.12 ± 7.10	151.2 ± 3.40	5805.2	29.14 ± 4.74
6 wt% Nb_2O_5/AZ31	20.35	84.64	61.04 ± 4.56	142.3 ± 3.15	5780.7	16.79 ± 3.98

3.4. Tensile Properties

The tensile curves (Figure 4a–d) of $Nb_2O_5/AZ31$ Mg MMCs at different stages of plastic deformation are shown to determine the engineering stress–strain curve. A summary of the mechanical properties of $Nb_2O_5/AZ31$ MMCs obtained through uniaxial tensile tests

is presented below in Table 3. This study shows that the ECAP plastic deformation process and the addition of Nb_2O_5 weight percentage remarkably influence the mechanical behavior of Nb_2O_5/AZ31 MMCs. The ultimate tensile strength of AZ31 composites increased from 131.7 MPa to 135.8 MPa (1 pass) and 138.5 MPa (2 passes) due to their improved performance. The ultimate tensile strength value of 3 wt% Nb_2O_5/AZ31 increased by 4.7% and 5.8% for one and two passes compared with the annealed composite. Similarly, the ultimate tensile strength value of 6 wt% Nb_2O_5/AZ31 increased by 5 % and 4% for and 1 and 2 passes compared with the aged composite.

(a)

(b)

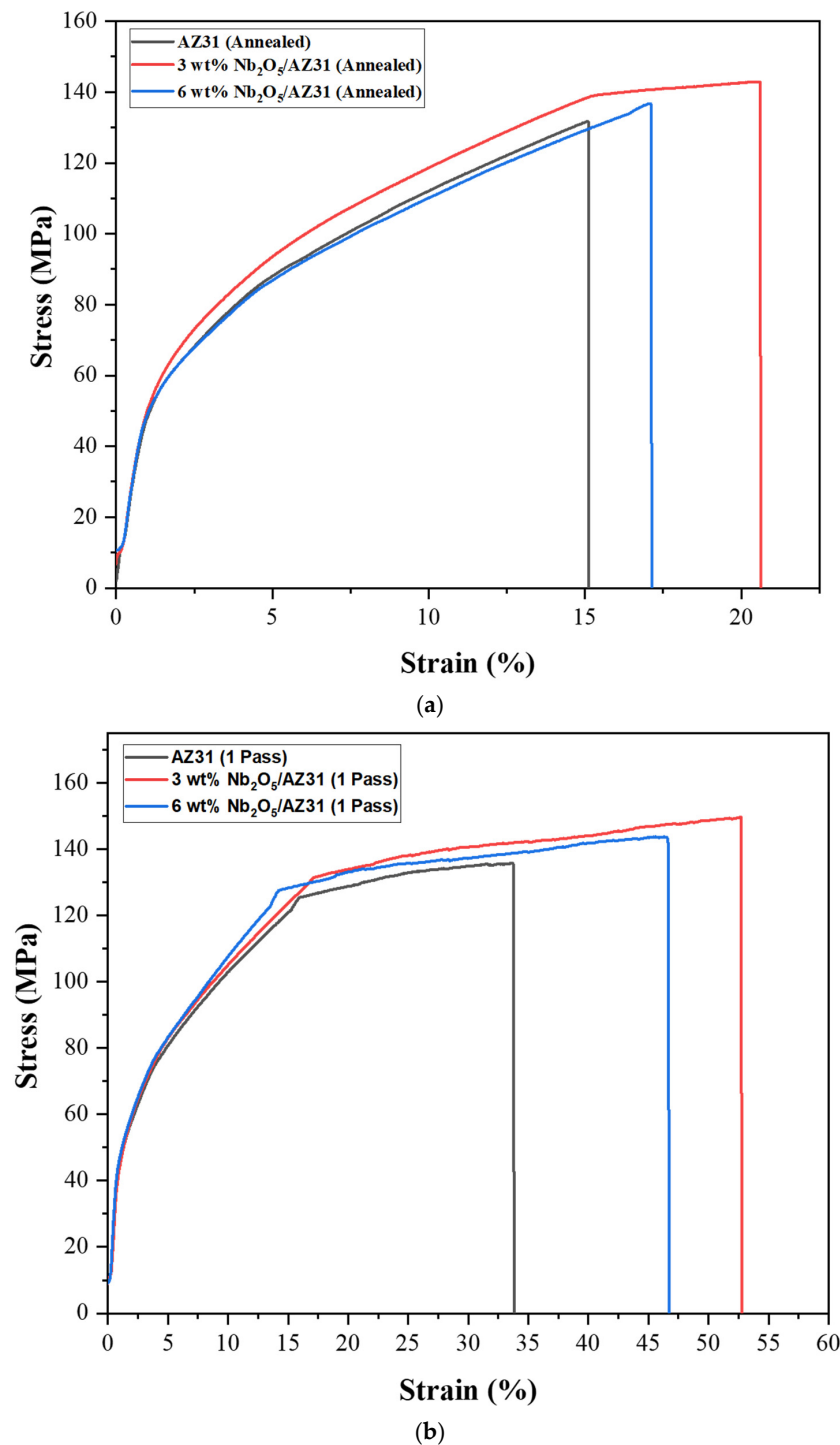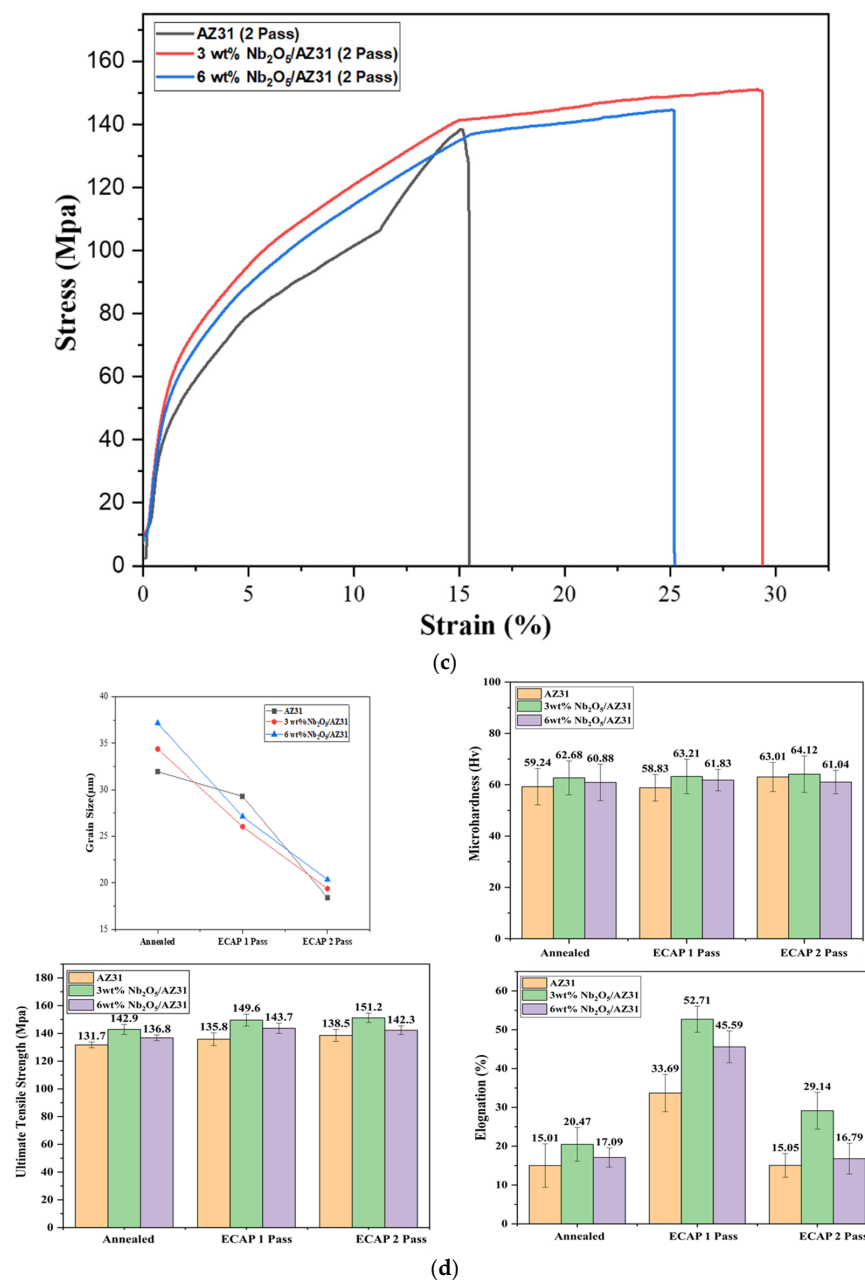**Figure 4.** *Cont.*

(c)

(d)

Figure 4. (**a**) Stress–strain curve under tension for annealed $Nb_2O_5/AZ31$ composites. (**b**) Stress–strain curve under tension for ECAPed 1-pass Nb2O5/AZ31 composites. (**c**) Stress–strain curve under tension for ECAPed 2-pass $Nb_2O_5/AZ31$ composites. (**d**) Comparison graph of grain size, microhardness, ultimate tensile strength, and elongation of $Nb_2O_5/AZ31$ composites.

4. Discussion

4.1. Microstructural Characteristics

Homogenization and subsequent aging treatment conditions resulted in the dissolution of a large amount of the second phase ($Mg_{17}(Al, Zn)_{12}$). A high processing temperature and a high strain rate during the preparation of the ECAP are believed to be responsible for this result [32]. The high plastic straining that occurs during the ECAP plastic deformation process results in improvements to the microstructure and mechanical characteristics of the material. The coarse grains were broken up because several pressings were performed, which led to a more uniform microstructure after two passes. Dynamic recrystallization occurs during this process because equiaxed grains may be observed in each pass of the ECAP process. However, it does not occur during the nucleation process or the formation

of new grains. When subjected to strain via ECAP, a microstructure that has been ECAPed gradually develops additional fine grains due to the straining effect. The ECAP microstructure transforms into a homogenous microstructure that is formed of fine grains and has high-angle boundaries because the subgrain boundaries can accommodate a considerable number of dislocations. From the SEM micrographs and XRD analysis, a remarkable relationship was observed between the grain size distribution and dislocation density of the samples. As shown in Figure 5d, the dislocation density increases with the decrease in particle size in the annealed and ECAP samples. The nucleation rate increases with the decrease in particle size, resulting in a decrease in the average grain size (or crystallite size). As shown in the results, the change in dislocation density with particle size is consistent [33]. Accordingly, more grains are observed in the microstructure, resulting in a high dislocation density value.
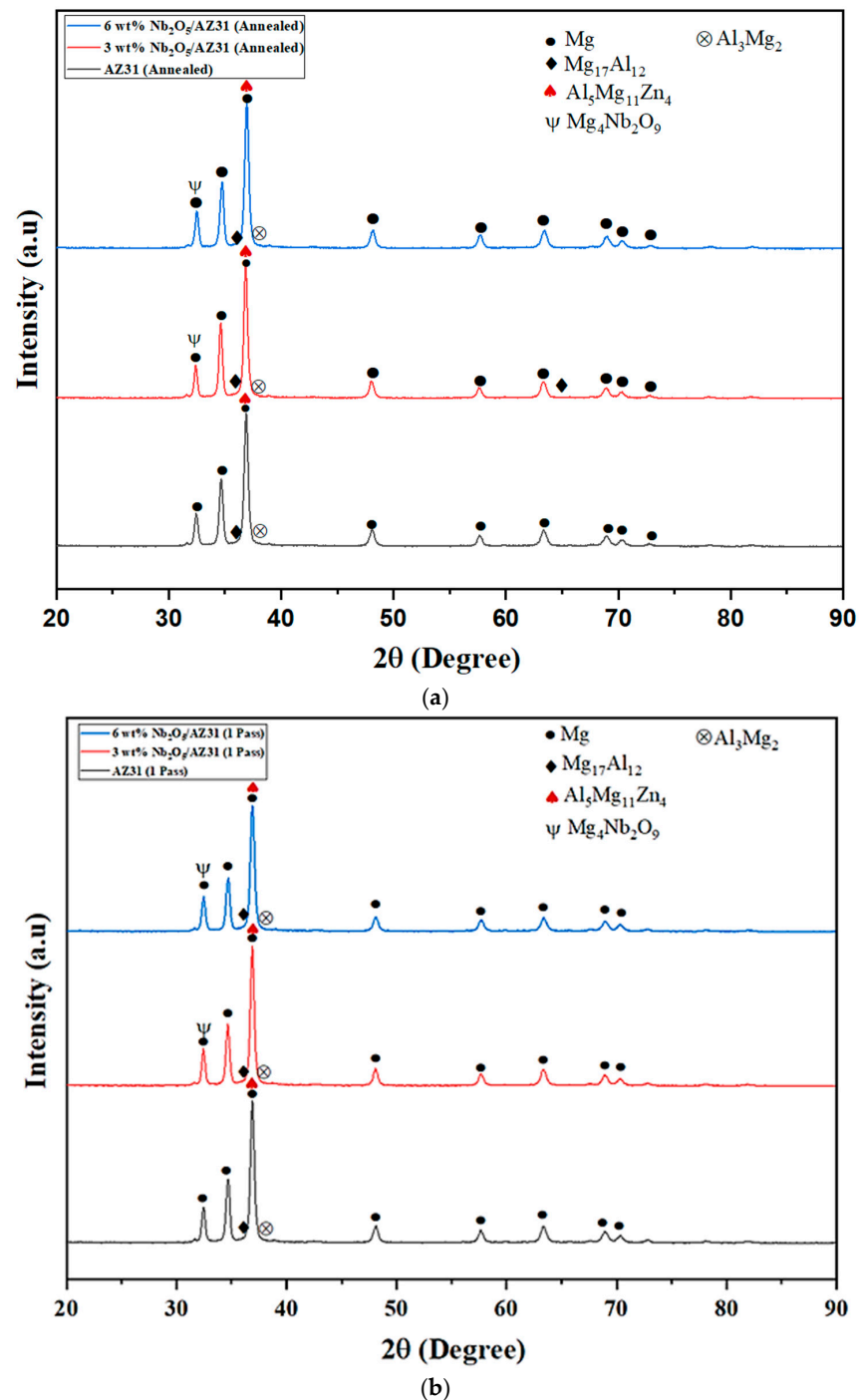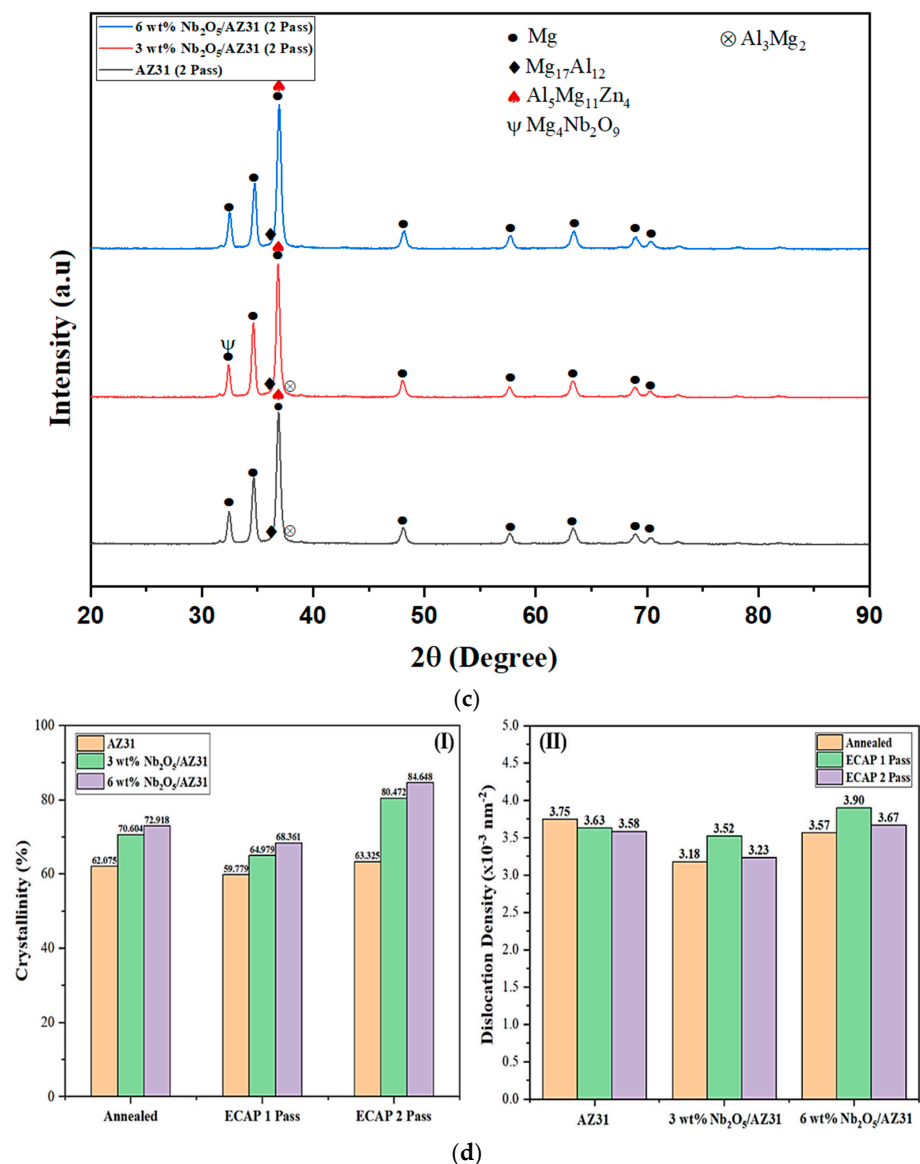

(a)

(b)

Figure 5. *Cont.*

Figure 5. (**a**) XRD pattern of the annealed samples. (**b**) XRD pattern of the ECAPed 1-pass samples. (**c**) XRD pattern of the ECAPed 2pass samples. (**d**) (**I**). Degree of crystallinity (**II**). Dislocation density.

4.2. XRD Analysis

The XRD results of the as-cast AZ31 alloy, 3 wt% Nb_2O_5/AZ31, and 6 wt% Nb_2O_5/AZ31 composites processed using ECAP are presented in Figure 5a–d. The ECAP has an effect on the types of phases that are characterized by peak intensity. In all stages of the ECAP process, the as-cast magnesium alloy AZ31 emerged as a single or multiphase system, with one Mg phase present in all of them. However, the quantitative XRD analysis indicated limited evidence for the presence of $Al_{12}Mg_{17}$, $Al_5Mg_{11}Zn_4$, and other Al–Mg phases at all stages of ECAP plastic deformation. During the casting of AZ31 alloy, a eutectic structure consisting of $Al_{12}Mg_{17}$ formed in the grain boundary due to the diffusion of Al and Zn elements into the composite. The eutectic structure of α-Mg+ MgZn totally disintegrated when the billets were subjected to heat treatment, and an icosahedral phase composed of $Al_5Mg_{11}Zn_4$ + α-Mg was formed at the grain boundaries [34]. The present study examined the low-symmetry (HCP) structure of the AZ31 alloy composite. The basal slip system [0 0 0 1] and <1 1 −2 0> could only be operated when ECAP was in operation [35]. The intensity of the [1 0 1 1] and [1 0 −1 2] planes increased after ECAP, which indicated that the dislocation slip is the main means of deformation during the passes [36,37]. An

irreversible dislocation slip can be generated in a crystal structure containing symmetry (HCP) structure, and the samples will deform plastically in this case [38]. The XRD experimental study showed that the plane intensity increased with the passing of the ECAP process with respect to the passes performed. Table 2 shows the formation of phases under different conditions of heat treatment and the diffusion of major phases based on their weight fractions. The quantitative analysis of the phases must be evaluated as accurately as possible. This condition is because the properties of a material are remarkably influenced by the varying weight fraction of the phase involved.

4.3. Mechanical Properties

4.3.1. Microhardness

The microhardness values of Nb_2O_5/AZ31 MMCs processed using ECAP are shown in Table 3. The composite's microhardness determines its strength and ductility. In general, microhardness and tensile strength are linearly correlated. Several researchers have found that the grain size decreases when the number of passes is increased [39]. The reduction in grain size occurred in tandem withs an increase in the hardness value and ductility. A similar increase in the microhardness of the Nb_2O_5/AZ31 composite was observed in the current study with the increase in the number of ECAP passes. The matrix grain size and agglomeration reduced because of the effects of Nb_2O_5 nanoparticles and ECAP plastic deformation, resulting in uniform microstructure distribution. An $Al_{12}Mg_{17}$ phase was formed because of the ECAP process, and the dissociation of different intermetallics was refined and distributed uniformly due to the grain refinement. The porosity of metal matrix composites increases with the percentage of reinforcements used. As a result, particle agglomeration results in porosity formation and removing agglomerates with increasing plastic deformation results in a reduction in porosity and an increase in interfacial bonding between matrix grains and reinforcement particles. It is possible to eliminate some air that is trapped within particle clusters during solidification by imposing plastic deformation upon them.

4.3.2. Tensile Properties

The grain refinement improved the mechanical properties due to SPD. The presence of Nb_2O_5 particles in the matrix acts as a nucleation surface during deformation, which prevents the dislocations from forming and refines the grain structure, thereby improving the strength of the material. The grain boundaries become more prominent due to the refinement of the grains, resulting in the formation of more hindrances, thereby decreasing the dislocation motion caused by the grain refinement [18]. Consequently, the dislocation density in the grain boundaries increases, which results in an increase in strength caused by the Hall–Petch mechanism [40]. Although Mg alloys exhibit a limited number of slip systems, deformation twinning can easily activate their HCP crystal structure at room temperature. The aluminum atoms will effectively interfere with the atomic shuffle that occurs during twinning due to their small size. Thus, the stress levels in the localized region caused by twinning remain the same. Orowan strengthening leads to twin bands due to twinning that occurs and propagates during stress concentration. The strength increase can be attributed to the Orowan strengthening and load-bearing effects of the reinforcements. When the composite is deformed under stress, the increased crystallinity of the matrix enhances the stress transfer between the matrix and reinforcement particles [32]. During deformation, AZ31 magnesium alloys exhibit a yield plateau caused by localized twinning. There is also a significant correlation between the yield plateau and grain size. The grain size decreases when the number of ECAP passes is increased. This may lead to a yield plateau being exhibited. Furthermore, the yield plateaus have been also related to the Lüders phenomenon. Stress–strain curves show a serrated pattern that may be due to the propagation of Lüders bands in the tensile specimen during testing. The Lüders phenomenon occurs when a material experiences localized deformation prior to macroscopically yielding. In the initial stages of tensile deformation, materials undergo

elastic deformation until their critical stress level is reached. Lüders bands form initially in localized areas as the material deforms plastically. As these bands spread throughout the specimen, the material undergoes uniform plastic deformation. The yield plateau appears on some materials' stress–strain curves. The stress stays relatively constant during the significant plastic deformation of the material. The material can sustain a relatively high stress level at this stage without significant strain. Plastic deformation occurs in the surrounding regions when Lüders bands propagate. The Lüders bands redistribute stresses within the material, so it can undergo significant plastic deformation while maintaining a nearly constant stress level. Lüders phenomena or yield plateaus are influenced by diverse material characteristics, including crystal structure, impurity level, and processing conditions. The SPD of the matrix results in strong interfacial bonds between the matrix and reinforcements, so that the properties of the composite are improved. Thus, high crystallinity correlates with higher ductility and strength.

4.3.3. Fractography

Fractographic analysis shows that the magnesium alloy composite breaks in aw brittle way because of its limited slip system. Figure 6a shows the fracture surface morphology of homogenized pure AZ31, which indicates mixed fracture facets, such as ductile and brittle in nature. The twinning transgranular fracture can be observed because of the limited slip planes of magnesium HCP crystal arrangement. The dimple diameter of AZ31 is less than the 3 wt% Nb_2O_5/AZ31, which might be the reason for the lower strength value. As shown in Figure 6b, more dimples were observed, but the cleavage facet led to the propagation of a microcrack, which was followed by brittle surface fracture. The introduction of 3 wt% Nb_2O_5 led to a clear improvement in dimple diameter and a remarkable improvement in tensile strength compared with pure AZ31. The precipitation of the secondary phase increased in the case of 6 wt% Nb_2O_5/AZ31, which is indicated by the grain boundary thickness in Figure 6c. The precipitate partial hotspot around the grain boundary might induce a stress–strain inhomogeneity, leading to an intergranular crack from a cleavage facet.
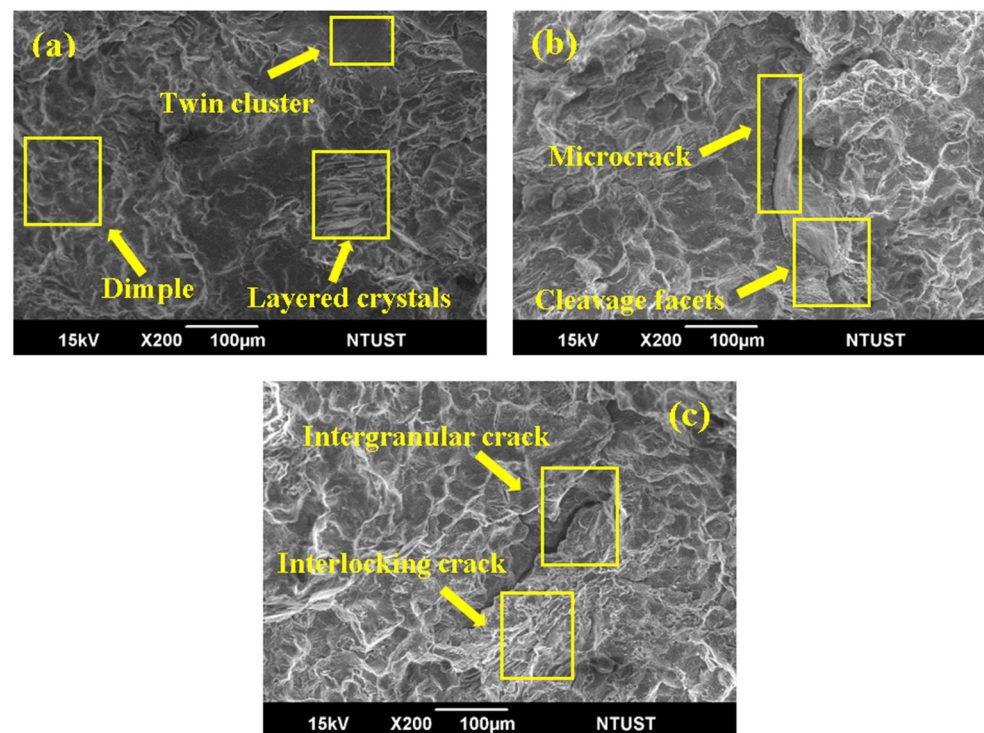

Figure 6. Fracture surface of annealed Nb_2O_5/AZ31 composites: (**a**) AZ31, (**b**) 3 wt% Nb_2O_5/AZ31, (**c**) 6 wt% Nb_2O_5/AZ31.

Figure 7a shows the brittle fracture characteristic of one ECAP-passed AZ31 magnesium alloy with typical fluted facets. The induction of micropores might be due to the oxygen inclusion, which can be a reason for the crack initiation or play an important role in crack propagation. The tensile strength value of 3 wt% Nb_2O_5/AZ31 shows the improvement by introducing reinforcement and ECAP followed by aging. In Figure 6b, the addition of reinforcement increased the dimple diameter. In Figure 7b, the crack surface is featured with uniform dimples. Compared with other fracture surfaces, no microcrack is induced, and brittle pattern cracking is minimal. The presence of precipitates helped improve the mechanical properties due to their decent distribution throughout the grains. The heat treatment and the number of ECAP passes favored the distribution of the secondary phase in this case. With a slight decrease in ultimate tensile strength, 6 wt% Nb_2O_5/AZ31 shows a wide variety of fracture morphology, such as micropores, dimples, microcracks, and fluted facets, as shown in Figure 7c. The second ECAP pass might lead to these multiple crack categories, and the formation of micropores can be the result of the β-$Mg_4Nb_2O_9$ phase. The chance of microcrack growth increases because of the coalescence of fluted facets and limited slip planes. Although the increase in dimple diameter can be observed, the localization of precipitates around the grain boundary might lead to an extremely small reduction in strength but increase the chance of crack induction due to the local inhomogeneity.
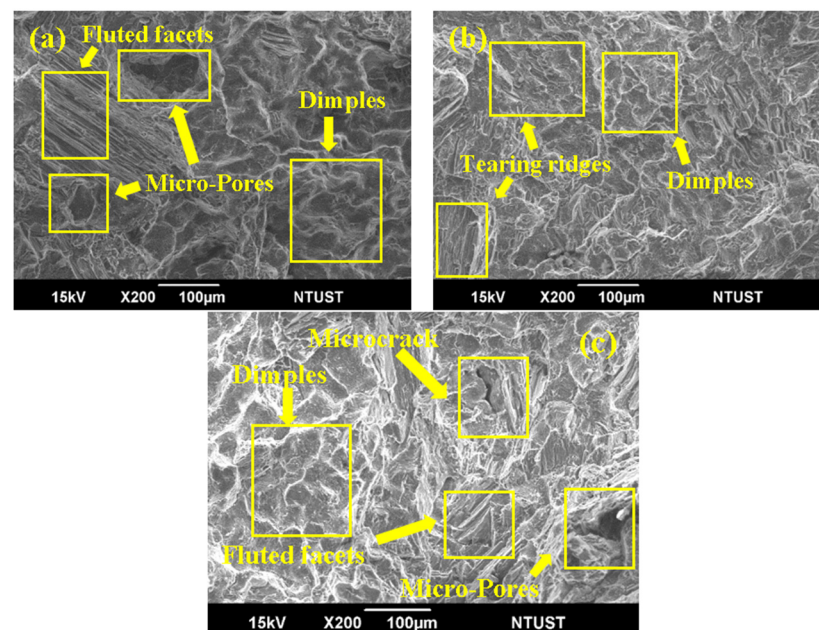

Figure 7. Fracture surface of ECAPed 1-pass Nb_2O_5/AZ31 composites: (**a**) AZ31, (**b**) 3 wt% Nb_2O_5/AZ31, (**c**) 6 wt% Nb_2O_5/AZ31.

With a comparative decrement in the tensile strength of 2-pass AZ31, the corresponding elongation decreased because of the microstructural change. An extremely lower percentage of dimples with considerable layered crystal fracture mechanics can observed by comparing Figures 7a and 8a. The decrease in dimple diameter and number signifies the reduction in ductility. As shown in Figure 8b, the 3 wt% Nb_2O_5 reinforcement shows considerable strength, but its ductility remarkably decreases when compared with one pass. The increased oxygen inclusion amount in Figure 8b might lead to the crack propagation. The tearing ridges can propagate from the generated pores due to the early-stage reinforcement nucleation. Several layered crystals with different slip plans can be observed, and the agglomeration of the layered crystal generates a cleavage facet and propagates toward the tearing ridges. As shown in Figure 8c, the morphology of 6 wt% Nb_2O_5/AZ31 consists of more depressive fracture mechanics due to shear bend and precipitate localization. The dimple count is mostly negligible, with the highest percentage of layered crystal. The incre-

ment in the secondary phase in 2-pass 6 wt% Nb_2O_5/AZ31 has good strength. However, the fracture morphology shows ductility reduction and has a wide variety of brittle fracture mechanics compared with other compositions and passes. Mg has an HCP structure with limited slip, so severe plastic deformation may result in local shear stress exceeding the metal's shear yield stress, causing void formation. Micro voids can be generated in highly strained regions, such as shear bands and cross twins, which can lead to a decrease in strength and ductility after one ECAP pass. The localization of precipitates near the grain boundary can add up with the shear bend and lead to a catastrophic failure of the material.
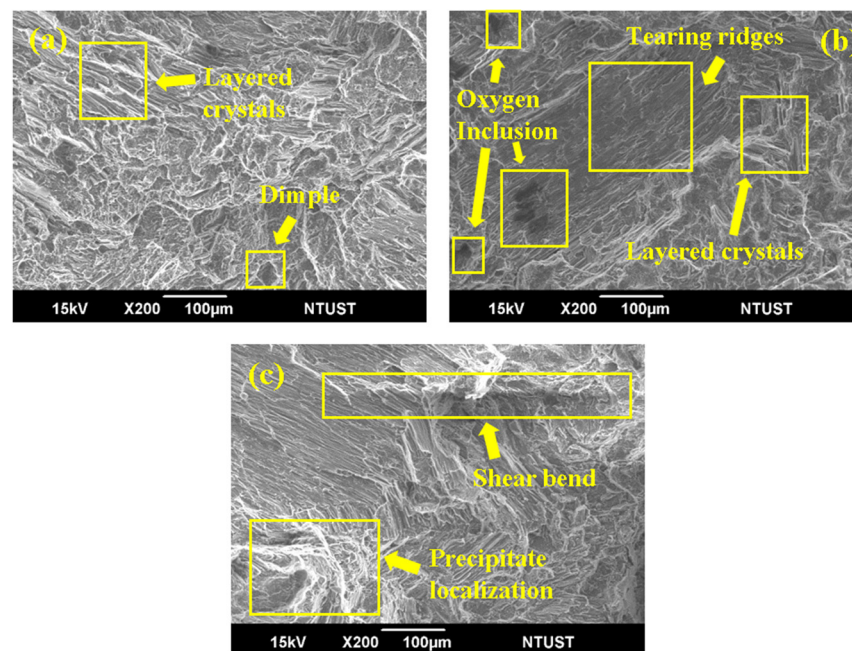

Figure 8. Fracture surface of ECAPed 2-pass Nb2O5/AZ31 composites: (**a**) AZ31, (**b**) 3 wt% Nb_2O_5/AZ31, (**c**) 6 wt% Nb_2O_5/AZ31.

5. Conclusions

This study focused on the microstructure and mechanical properties of Nb_2O_5/AZ31 composites subjected to an SPD (ECAP) process. The conclusions are summarized as follows:

- The Nb_2O_5/AZ31 ECAPed composites had remarkably reduced grain size when compared with the aged composites, and the microstructures of the composites contained mostly α-magnesium.
- On the basis of the XRD results, the intensity of the [1 0 1 1] and [1 0 −1 2] planes increased, indicating that the dislocation slip is the main means of deformation during each pass, leading to a reduction in porosity.
- With an increasing number of passes, the microhardness value increased, and the maximum microhardness value was reached, which was 64.12 HV for a 3 wt% of Nb_2O_5/AZ31.
- In accordance with the tensile results, the ultimate tensile strength of the ECAPed Nb_2O_5/AZ31 composites remarkably increased compared with the annealed AZ31 composite. With the increase in the number of passes, the mechanical properties of the composites began to increase, and the maximum ultimate tensile strength value was reached, which was 151.2 MPa for a 3 wt% of Nb_2O_5/AZ31 (two passes).

References

1. Nie, K.B.; Wang, X.J.; Deng, K.K.; Hu, X.S.; Wu, K. Magnesium Matrix Composite Reinforced by Nanoparticles—A Review. *J. Magnes. Alloys* **2021**, *9*, 57–77. [CrossRef]
2. Song, J.; Chen, J.; Xiong, X.; Peng, X.; Chen, D.; Pan, F. Research Advances of Magnesium and Magnesium Alloys Worldwide in 2021. *J. Magnes. Alloys* **2022**, *10*, 863–898. [CrossRef]
3. Chen, X.; Zhang, D.; Xu, J.; Feng, J.; Zhao, Y. Improvement of Mechanical Properties of Hot Extruded and Age Treated Mg–Zn–Mn–Ca Alloy through Sn Addition. *J. Alloys Compd.* **2021**, *850*, 156711. [CrossRef]
4. Yang, Y.; Xiong, X.; Chen, J.; Peng, X.; Chen, D.; Pan, F. Research Advances in Magnesium and Magnesium Alloys Worldwide in 2020. *J. Magnes. Alloys* **2021**, *9*, 705–747. [CrossRef]
5. Dey, A.; Pandey, K.M. Magnesium Metal Matrix Composites—A Review. *Rev. Adv. Mater. Sci.* **2015**, *42*, 58–67.
6. Kulekci, M.K. Magnesium and Its Alloys Applications in Automotive Industry. *Int. J. Adv. Manuf. Technol.* **2008**, *39*, 851–865. [CrossRef]
7. Huang, S.J.; Ali, A.N. Effects of Heat Treatment on the Microstructure and Microplastic Deformation Behavior of SiC Particles Reinforced AZ61 Magnesium Metal Matrix Composite. *Mater. Sci. Eng. A* **2018**, *711*, 670–682. [CrossRef]
8. Sepahi-Boroujeni, S.; Sepahi-Boroujeni, A. Improvements in Microstructure and Mechanical Properties of AZ80 Magnesium Alloy by Means of an Efficient, Novel Severe Plastic Deformation Process. *J. Manuf. Process.* **2016**, *24*, 71–77. [CrossRef]
9. Zhou, T.; Zhang, Q.; Li, Q.; Wang, L.; Li, Q.; Liu, D. A Simultaneous Enhancement of Both Strength and Ductility by a Novel Differential-Thermal ECAP Process in Mg-Sn-Zn-Zr Alloy. *J. Alloys Compd.* **2022**, *889*, 161653. [CrossRef]
10. Shen, M.J.; Wang, X.J.; Ying, T.; Wu, K.; Song, W.J. Characteristics and Mechanical Properties of Magnesium Matrix Composites Reinforced with Micron/Submicron/Nano SiC Particles. *J. Alloys Compd.* **2016**, *686*, 831–840. [CrossRef]
11. Bains, P.S.; Sidhu, S.S.; Payal, H.S. Fabrication and Machining of Metal Matrix Composites: A Review. *Mater. Manuf. Process.* **2016**, *31*, 553–573. [CrossRef]
12. Zhao, K.N.; Li, H.X.; Luo, J.R.; Liu, Y.J.; Du, Q.; Zhang, J.S. Interfacial Bonding Mechanism and Mechanical Properties of Novel AZ31/WE43 Bimetal Composites Fabricated by Insert Molding Method. *J. Alloys Compd.* **2017**, *729*, 344–353. [CrossRef]
13. Idrisi, A.H.; Mourad, A.H.I. Conventional Stir Casting versus Ultrasonic Assisted Stir Casting Process: Mechanical and Physical Characteristics of AMCs. *J. Alloys Compd.* **2019**, *805*, 502–508. [CrossRef]
14. Dinaharan, I.; Zhang, S.; Chen, G.; Shi, Q. Assessment of Ti-6Al-4V Particles as a Reinforcement for AZ31 Magnesium Alloy-Based Composites to Boost Ductility Incorporated through Friction Stir Processing. *J. Magnes. Alloys* **2022**, *10*, 979–992. [CrossRef]
15. Huang, S.-J.; Subramani, M.; Chiang, C.-C. Effect of Hybrid Reinforcement on Microstructure and Mechanical Properties of AZ61 Magnesium Alloy Processed by Stir Casting Method. *Compos. Commun.* **2021**, *25*, 100772. [CrossRef]
16. Safavi, M.S.; Walsh, F.C.; Visai, L.; Khalil-Allafi, J. Progress in Niobium Oxide-Containing Coatings for Biomedical Applications: A Critical Review. *ACS Omega* **2022**, *7*, 9088–9107. [CrossRef]
17. Chen, J.; Jiang, X.; Lyu, L.; Li, Y.; Christian, P.; Sun, H.; Shu, R. Microstructures and Mechanical Properties of Nano-C and In Situ Al_2O_3 Reinforced Aluminium Matrix Composites Processed by Equal-Channel Angular Pressing. *J. Alloys Compd.* **2021**, *876*, 160159. [CrossRef]
18. Zhou, W.; Lin, J.; Dean, T.A. Microstructure and Mechanical Properties of Curved AZ31 Magnesium Alloy Profiles Produced by Differential Velocity Sideways Extrusion. *J. Magnes. Alloys* **2023**, *11*, 493–508. [CrossRef]
19. Abbas, A.; Huang, S.J. Investigation of Severe Plastic Deformation Effects on Microstructure and Mechanical Properties of WS2/AZ91 Magnesium Metal Matrix Composites. *Mater. Sci. Eng. A* **2020**, *780*, 139211. [CrossRef]
20. Polly, P.; Chandra Sekhar, K.; Ravisankar, B.; Kumaran, S. Densification of Mechanically Alloyed Al5083-5wt% Y_2O_3 Nano-Composite by Equal Channel Angular Pressing. *Appl. Mech. Mater.* **2014**, *592–594*, 963–967. [CrossRef]
21. Feng, A.H.; Ma, Z.Y. Enhanced Mechanical Properties of Mg-Al-Zn Cast Alloy via Friction Stir Processing. *Scr. Mater.* **2007**, *56*, 397–400. [CrossRef]
22. Qiao, X.G.; Ying, T.; Zheng, M.Y.; Wei, E.D.; Wu, K.; Hu, X.S.; Gan, W.M.; Brokmeier, H.G.; Golovin, I.S. Microstructure Evolution and Mechanical Properties of Nano-SiCp/AZ91 Composite Processed by Extrusion and Equal Channel Angular Pressing (ECAP). *Mater. Charact.* **2016**, *121*, 222–230. [CrossRef]
23. Figueiredo, R.B.; Langdon, T.G. Principles of Grain Refinement and Superplastic Flow in Magnesium Alloys Processed by ECAP. *Mater. Sci. Eng. A* **2009**, *501*, 105–114. [CrossRef]

24. Meredith, C.S.; Khan, A.S. The Microstructural Evolution and Thermo-Mechanical Behavior of UFG Ti Processed via Equal Channel Angular Pressing. *J. Mater. Process. Technol.* **2015**, *219*, 257–270. [CrossRef]
25. Minárik, P.; Máthis, K.; Ku, R. Influence of Equal Channel Angular Pressing Routes on Texture, Microstructure and Mechanical Properties of Extruded AX41 Magnesium Alloy. *Mater. Charact.* **2017**, *123*, 282–293. [CrossRef]
26. Avvari, M.; Narendranath, S.; Nayaka, H.S. Effect of Processing Routes on AZ31 Alloy Processed by Severe Plastic Deformation. *Procedia Mater. Sci.* **2014**, *5*, 1560–1566. [CrossRef]
27. Jeong, H.T.; Kim, W.J. Critical Review of Superplastic Magnesium Alloys with Emphasis on Tensile Elongation Behavior and Deformation Mechanisms. *J. Magnes. Alloys* **2022**, *10*, 1133–1153. [CrossRef]
28. Huang, S.J.; Ali, A.N. Experimental Investigations of Effects of SiC Contents and Severe Plastic Deformation on the Microstructure and Mechanical Properties of SiCp/AZ61 Magnesium Metal Matrix Composites. *J. Mater. Process. Technol.* **2019**, *272*, 28–39. [CrossRef]
29. Song-jeng, H.; Sathiyalingam, K.; Murugan, S. Effect of Nano-Nb_2O_5 on the Microstructure and Mechanical Properties of AZ31 Alloy Matrix Nanocomposites. *Adv. Nano Res. Int. J.* **2022**, *4*, 407–416. [CrossRef]
30. Huang, S.J.; Subramani, M.; Borodianskiy, K. Strength and Ductility Enhancement of $AZ61/Al_2O_3/SiC$ Hybrid Composite by ECAP Processing. *Mater. Today Commun.* **2022**, *31*, 103261. [CrossRef]
31. Jeon, S.; Liu, X.; Azersky, C.; Ren, J.; Zhang, S.; Chen, W.; Hyers, R.W.; Costa, K.; Kolbe, M.; Matson, D.M. Particle Size Effects on Dislocation Density, Microstructure, and Phase Transformation for High-Entropy Alloy Powders. *Materialia* **2021**, *18*, 101161. [CrossRef]
32. Cheng, J.; Zhao, J.H.; Zheng, D.; He, K.; Guo, Y. Effect of the Vacuum Heat Treatment on the Microstructure and Mechanical Properties of the Galvanized-Q235/AZ91D Bimetal Material Produced by Solid–Liquid Compound Casting. *Met. Mater. Int.* **2021**, *27*, 545–555. [CrossRef]
33. Pei, Z.; Sheng, H.; Zhang, X.; Li, R.; Svendsen, B. Tunable Twin Stability and an Accurate Magnesium Interatomic Potential for Dislocation-Twin Interactions. *Mater. Des.* **2018**, *153*, 232–241. [CrossRef]
34. Yoo, M.H. Slip, Twinning, and Fracture in Hexagonal Close-Packed Metals. *Metall. Trans. A* **1981**, *12*, 409–418. [CrossRef]
35. Du, C.; Gao, Y.; Hua, Z.M.; Zha, M.; Wang, C.; Wang, H.Y. Enhanced Superplasticity Achieved by Disclination-Dislocation Reactions in a Fine-Grained Low-Alloyed Magnesium System. *Int. J. Plast.* **2022**, *154*, 103300. [CrossRef]
36. Wang, F.; Agnew, S. Dislocation-Twin Interactions in Magnesium Alloy AZ31. In *Magnesium Technology 2015*; Springer: Cham, Switzerland, 2015; pp. 139–144. [CrossRef]
37. Muralidhar, A.; Narendranath, S.; Shivananda Nayaka, H. Effect of Equal Channel Angular Pressing on AZ31 Wrought Magnesium Alloys. *J. Magnes. Alloys* **2013**, *1*, 336–340. [CrossRef]
38. Hall, E.O. The Deformation and Ageing of Mild Steel: III Discussion of Results. *Proc. Phys. Soc. B* **1951**, *64*, 747. [CrossRef]
39. Emadi, P.; Andilab, B.; Borodianskiy, K.; Ravindran, C. Strengthening of Mg-Al-Zn-Mn Alloy Using SiC/Al Nanocomposite Extrusion. *J. Alloys Compd.* **2022**, *922*, 166243. [CrossRef]
40. Agnew, S.R.; Calhoun, C.A.; Bhattacharyya, J.J. What is in A strain hardening "plateau". In *Magnesium Technology 2016*; Springer: Cham, Switzerland, 2016; Volume 5, pp. 189–194.